RHESSI Aspect System and In-flight Calibration

Martin Fivian[a], Reinhold Henneck[a], Alex Zehnder[a]
and the RHESSI Team[a,b,c]

[a]Paul Scherrer Institute, CH-5232 Villigen, Switzerland
[b]Goddard Space Flight Center, Greenbeld MA, USA
[c]Space Sciences Laboratory, UC-Berkeley, USA

ABSTRACT

Precise knowledge of the pointing and the roll angle of the rotating spacecraft is needed in order to reconstruct images with 2 arcsec resolution using the modulation patterns seen on each of the detectors of the bi-grid rotating collimators. Therefore, the aspect system consists of two subsystems of sensors, the Solar Aspect System (SAS) and Roll Angle System (RAS). The transmitted data consists of Solar limb data from the SAS (CCD pixels around the intersection of a Solar image with three linear CCDs) and Star event data from the RAS (CCD pixels induced by passages of Star images over a linear CCD). In order to meet the RHESSI requirements, the reconstructed pointing needs to be ≤ 0.4 arcsec (rms) relatively (≤ 1 arcsec absolutely) and the determination of the roll angle needs to be better than 1 arcmin (rms). Beside of understanding and calibrating each sensor, the error budget on the aspect system requires an alignment of the relevant features of the 1.55 m extended telescope on a micron level. This could be achieved by a combination of on-ground and in-flight calibration.

Keywords: solar aspect system, roll angle system, star scanner, star tracker, optical imaging, Sun sensor, CCD

1. INTRODUCTION

The Reuven Ramathy High Energy Solar Spectroscopic Imager (RHESSI) is a small explorer mission that has been launched by NASA on Feb. 5, 2002 into a circular low earth orbit (600 km altitude, 38 degrees inclination).[1] The primary scientific aim of the mission is to investigate the physics of particle acceleration and energy release in solar flares. RHESSI observes the full Sun with an unprecedented combination of spatial resolution (between 2.3 and 35 arcsec) and energy resolution (1 keV to 5 keV) in the energy range from 3 keV to 17 MeV. The single instrument on a spin stabilized spacecraft utilizes Fourier-transform[2] imaging with 9 bi-grid rotating modulation collimators[3] spaced at 1.55 m and 9 cooled germanium detectors.[4,5]

Since the transmission probability for a photon through the collimators depends on the incident angle with respect to the telescope axis, and because the spacecraft can only be controlled on a arcmin level, the spatial resolution depends critically on a precise knowledge of the momentary pointing direction and roll angle. In order to have a spatial resolution of 2.3 arcsec (for the finest grids) and to precisely correlate with observations at other wavelengths two precise aspect systems are implemented, the Solar Aspect System (SAS) and the Roll Angle System (RAS). The SAS yields sub-arcsec knowledge of the radial pointing with respect to the Sun center and the RAS provides precise knowledge on the roll angle of the rotating spacecraft (15 rpm). The combined SAS/RAS aspect system provides a knowledge of the absolute pointing with an accuracy of 1 arcsec.

The design and the alignment of the RHESSI imager, i.e. the telescope tube with the grids and SAS/RAS aspect optics and sensors, are discussed in Ref. 6 and 7. While the reconstruction of the aspect solution and the influence to the off-line imaging process is discussed in detail in Ref. 8 and 9, the presented paper concentrates on the performance and calibration of the aspect system.

Further author information: (Send correspondence to Martin Fivian)
Martin Fivian: E-mail: mfivian@ssl.berkeley.edu, Telephone: +1-510-643-0158
Alex Zehnder: E-mail: Alex.Zehnder@psi.ch, Telephone: +41-56-310-3615

2. SOLAR ASPECT SYSTEM (SAS)

2.1. SAS principles

The SAS consists of a set of 3 identical lens/sensor subsystems spaced at 120 degrees. Each subsystem consists of a 4 cm diameter lens located on the front grid tray of the imager tube that focuses a solar optical image onto a 2048-element x $(13\mu)^2$ linear CCD located on the rear grid tray. The focal length, given by the length of the imager tube, is 1.55 m resulting in a plate scale of 1.73 arcsec/pixel. In order to reduce chromatic aberration a bandpass filter at 670 nm with 12 nm bandwidth (FWHM) has been used. While each of the three CCDs are sampling solar profiles with 128 Hz using a programmable integration time between 0.02 and 2 ms, the digitized signal is sent to the aspect data processor (ADP) where a hardware programmed algorithm triggers 1 or several pixels around the solar limb using an adjustable threshold. Typically 4 pixels for each of the 6 limbs are written to the telemetry packets using a 8 or 10 bit resolution.

The transmitted data of each of the 6 Solar limbs are processed off-line by the ground based analysis software, where the position on the CCDs for each limb is determined. For ideal circumstances and with exactly known positions (lens optical center, CCD pixel location), the mid-perpendicular of the three chords, i.e. the straight line between the two limbs on each CCD, would intersect in one point, the momentary position of the Sun center. Given the accuracy of our dimensional measurements and given thermal and mechanical instabilities, the mid-perpendiculars usually do not intersect in one point but form a residual triangle. The best guess for the Sun center is then the center of gravity of the three intersects of the mid-perpendiculars.

The in section 2.4 is shows that the error budget of a relative pointing error of $\sigma \leq 0.4$ arcsec can easily be achieved by the implemented system.

2.2. CCD characterization

In order to optimize the accuracy of the limb determination and at the same time keeping the data rate acceptable, the front-end electronics has been tuned to have a low and constant (over pixel range and time) noise (≤ 1 mV), a stable dark signal and a stable, pixel-independent gain. Since the Sun center is determined from the average of the two limb positions on each CCD, effects due to a potential non-linearity of the signal response cancel in first order.

Most lab tests have been performed using a simulated Sun image (a Xenon arc lamp followed by a condenser and a 670 nm bandpass filter at room temperature.[10] The sensitivity has been checked by illuminating the CCD with an attenuated lab Sun, which has been calibrated by using a calibrated photo-diode. The result is compatible with the CCD specification to within 30%. Moreover, the measured sensitivity of the whole SAS system including lenses and filters agreed with expectation on a level of about 20% (see below).

2.2.1. Dark signal

The dark signal is the output signal in the absence of light and originates mainly from integrated dark leakage current and thermodynamic noise. Its amplitude can be influenced by the photo-gate voltage which however also affects the odd-even effect (see below) and thus was adjusted for a reasonable compromise. Fig. 1a shows the dark signal for SAS 2 at a typical operating temperature of about 20 degreeC for the electronic box. The pixel averaged dark signal was ≤ 2.5 mV for all CCDs measured and was found to depend very little on temperature; i.e. the maximum variation observed was 2 mV over the range from 0 to 55 degreeC. This clearly deviates from the usual dark signal dependence which states that the dark signal doubles for every 7 degreeC increase in temperature. The most surprising feature is the pixel-to-pixel non-uniformity within certain pixel regions. However, one can easily correct for this behavior since the dark signal characteristics is very stable.

2.2.2. Noise

The full system noise for the dark signal is between 0.4 mV to 0.6 mV (rms) and represents the average of the individual pixel rms values as a function of time (see Fig. 1b). This is below the ADC resolution to be used (≥ 1 mV/ch) and will therefore only have a negligible influence on the SAS performance. The noise values are roughly consistent with the value of 1 mV given by CCD manufacturer Loral for the peak-to-peak temporal noise, if one bears in mind that our ADC resolution is 0.5 mV/ch. It corresponds to roughly 370 electrons using a typical voltage-to-charge conversion factor of 1.2 μV/e- given by the output node capacity.
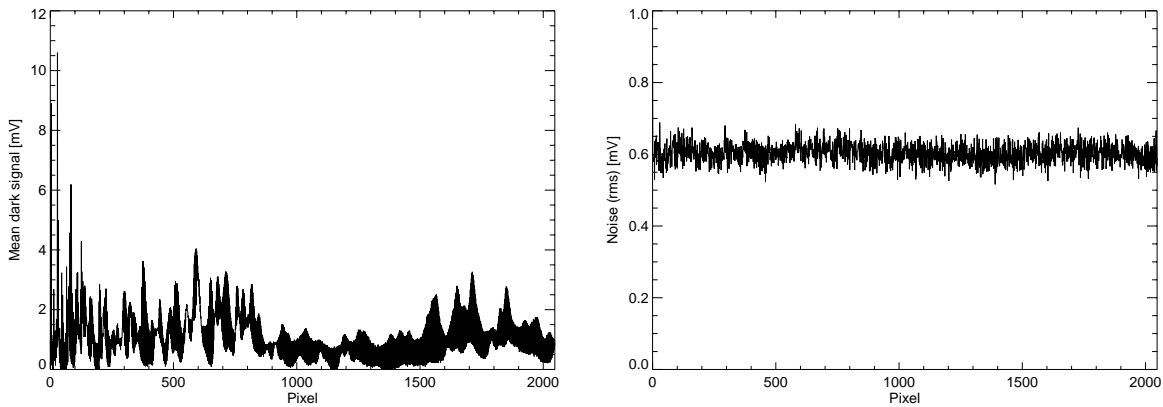
Figure 1. The left plot shows the mean dark signal for SAS 2. Although the dark signal is not uniform over the pixel range, it is stable in position and time. The right plot shows the noise (rms) of SAS 2. The results for SAS 1 and 3 are similar.

2.2.3. Hot and cold pixels

A hot (cold) pixel is a pixel the response of which is permanently above (below) a certain, critical high (low) threshold. To test for these pixels, the entire CCD areas has been illuminated with moderate intensity (around 100 mV). Using a high (low) threshold of about 1000 (50) mV no such pixels were found for all four flight CCDs.

2.2.4. Odd-even effect

'Odd-even' or 'register imbalance' describes the fact that odd and even pixels may have a different gain factor and respond in a typical staggering pattern to a uniform light input. Its cause is usually related to the fact that the charges for the odd and even pixel are shifted out via separate shift registers on either side of the central photo-site line, but are converted to voltages in the same pre-amplifier. Here, two effects must be considered separately: a 'global' pixel-independent odd-even effect and a 'local', pixel-dependent one.

The global odd-even effect varied considerably from CCD to CCD (by up to a factor 10) and was observed to be as large as $\Delta_{norm} = 2 \cdot (<\text{odd}> - <\text{even}>) / (<\text{odd}> + <\text{even}>) \leq 0.05$ after implementation of the pre-integration scheme.[7] This value is consistent with the specifications. It was also found that the odd-even effect could be minimized to some extent by selecting the photogate voltage which however also determined the amplitude of the dark signal amplitude. If always the same pixel regions were illuminated the odd-even differences $\Delta = <\text{odd}> - <\text{even}>$ were found to be a linear function of the mean amplitude $(<\text{odd}> + <\text{even}>)/2$, however with finite offsets at amplitude zero.

Therefore, a correction should be applicable (see also Ref. 11) if it were not for the presence of the local odd-even effect. The latter means that illuminating certain regions of the CCD affects the gain of either all the even or all the odd pixels. For instance, illuminating the pixel area around pixel 1850 raises the amplitude of all even pixels by about 0.8%. The effect depends critically on the illumination geometry and is enhanced by using light with more infrared components. This is caused presumably by illuminating certain areas of the transfer gates and of the odd or even shift registers lying on opposite sides of the central photo-diode line which are not deeply enough embedded so that light can penetrate and create additional charges in the odd or even shift register. Thus, the wavelength dependence of the local odd/even effect becomes plausible when bearing in mind that the absorption length of Si in the visible/IR region increases with increasing wavelength. Similar findings have been reported in the literature.[12] With the pre-integration scheme implemented the local odd-even effects could be reduced to $\Delta_{norm} \leq 0.01$ at maximum and typically $\Delta_{norm} \leq 0.005$. At low temperature (below 20 degreeC, far away from the specified range 10 degreeC to 30 degreeC), the local odd-even effect was found to increase dramatically (up to $\Delta \approx 100$ mV).

2.2.5. Gain homogeneity

Gain differences at the locations of the two limbs would produce a distorted Sun profile which combined with a common threshold value for both limbs would yield an incorrect determination of the center. In principle, the effect can be measured and the data can be corrected for since RHESSI rotates sufficiently fast. In the lab the issue was studied by moving the CCD in front of the light source which was limited in this case to illuminate only about 400 pixels and analyzing the average gain as a function of position. In this way the illumination geometry remained approximately constant for the different measurements. The resulting gain vs. position distributions are dominated by random effects and show only a very weak correlation which is consistent with a maximum linear gain variation of $\leq 6\%$ over the full pixel range.

2.2.6. Linearity

The linearity of the light response has been measured over the full dynamic range using the lab Sun and varying the integration time between 0.2 ms and 2 ms. The average dark signal collected over the non-illuminated pixels has been subtracted for the analysis of the illuminated pixels. The system showed no significant non-linearities.

2.2.7. CCD driven errors

The resulting error of the reconstructed pointing can be traced back to the following three different sources.

- uncertainties in the measurement on a single CCD

- uncertainties in the co-alignment of all the SAS features

- uncertainties in the co-alignment of the SAS with respect to the grids

While the co-alignment of the different features of the imager is discussed below, the CCD driven errors has been simulated and are presented here. Simulating the CCD response according to a Solar profile for the given optics, all the uncertainties due to the given CCD characteristics (sections 2.2.1 to 2.2.6) have to be applied. Introducing any random error in the measured Solar profile will result in a displacement of the limb position. Since the profile of the limb, the limb darking function convoluted with the point spread function of the SAS optics, is sampled constantly with a high rate, the profile will be sufficiently well known. Thus, a perfect limb profile has been assumed for the simulations. In order to estimate an upper limit for the error of the measured limb position, the following worst case values (rms) have been assumed: noise of 4 channels, gain uncertainty of 3%, error in dark signal of 8 channels, odd-even effect of 3%. All simulations showed an error of the limb fit of the order of 0.1 arcsec with more or less comparable contributions from all of the four factors. Takeing into account that the SAS is measuring six limbs with the geometry described above (see also Fig. 2), the expected relative pointing error due to the sensors is in the order of 0.05 arcsec and therefore negligable concerning the error budget of 0.4 arcsec (rms).

2.3. Ground calibration

For on-ground calibration, the imager with the integrated SAS subsystem (the lenses on the front tray and the SAS electronic box on the rear tray) was operated with its ground support equipment and pointed directly at the Sun. Setting an initial pointing slightly ahead of the Sun image motion, the drift of the Sun over the field of view (≈ 1 degree) gives a well defined trajectory in the SAS image plane. Full CCD readouts (SAS images) has been aquired with a cadence of up to 32 Hz and SAS limbs (four or more pixels around the solar limb) could be stored with the highest cadence of 128 Hz.[13]

The width of the solar limb, i.e. the angle over which the intensity raises from zero to about 50% of the maximum intensity (for images taken at 670 nm), is in the order of 1/100 arcsec. Therefore, the measured width is a function of diffraction, chromatic aberration, environmental and instrumental influences. Fitting the limbs with an error function adding a linear background gives a well defined width and position of the measured limb. The expected width of the point spread function of the SAS optics is 1.9 arcsec (rms). Therefore, the typically measured width of the limbs of 2.5 arcsec leads to a remaining broadening of 1.7 arcsec which is a realistic upper limit for the atmospheric 'seeing'.

2.4. Flight calibration

2.4.1. Measuring the alignment
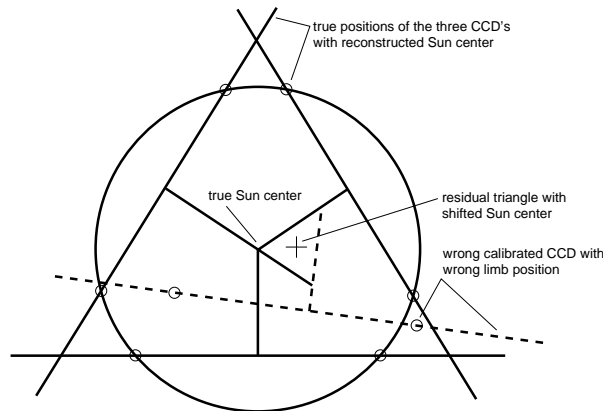
Figure 2. The circle indicates the Solar limb and the solid lines are at the true positions of the CCDs with the corresponding reconstruction of the Sun center. A wrong calibration of the position of a CCD leads to a residual triangle in the reconstruction and therefore a shifted, wrong reconstructed Sun center as shown with the dashed lines.

Measuring the positions of the six limbs at any given time, the position of the Sun center in the SAS image plane can be reconstructed. In general, the three mid-perpendiculars on the three chords do not intersect in one point as has been pointed out in section 2.1. Fig. 2 illustrates the geometry of the SAS for perfectly aligned CCDs and with an arbitray offset of one of the CCDs resulting in a residual triangle. The size and shape of the triangle depend sensitively on the relative position of lenses and CCDs. Therefore, the time series of the six measured radii and the residual triangle form a set of not self-consistent paramters which can be used for calibration of the relative SAS pointing. The calibration algorithm, which has has been published in Ref. 13, has been slightly modified to avoid any ambiguities when minimizing the size of the trianlge and has been applied as follows:

1. Assume that lens/CCD no. 1 is in correct position.

2. Minimize the variance of the size of the residual triangle by varying the two undefined angles.

3. Rotate the system to make the average offset of the angles zero.

4. Minimize the size of the residual triangle by varying the position of three CCDs symetrically in the direction of the CCDs.

5. Minimize the variance of the radii by varying the position of the three CCDs in the perpendicular direction.

6. Adjust the three plate scale to match the effective Solar radius.

Applying the above calibration algorithm, only a relative calibration of the SAS features (positions of the lenses and CCDs) can be achieved. The detailed pre-launch mechanical and optical measurements[7] are a good starting point for the optimization tasks which have to define offsets to the SAS feature in the imaging coordinate system. This coordinate system is defined using the nominal positions of the SAS features only. Since the lenses are mounted on the front tray on the same plane as the front grids and the SAS CCDs are fixed on the rear tray to be located in the same plane as the rear grids, any re-calibration of the SAS features does not effect the SAS/grid cross calibration (absolute SAS calibration) as long as the additional degree of freedom of the above alorithm is used to conserve the defined imaging coordinate system.

A scan of the parameter space showed that the minimization problems are absolutely non-ambiguous and the parameters can be fitted better than the required accuracy. The deviations from the ground based measurements are in the order of 10 μm or better for the relative positions between front and rear tray with one exeption. One of the three CCDs seems to be shifted by two pixels (within 0.2 μm) which is most likely due to a glitch in the synchronization of the first pixel in one of the FPGA programs. After the calibration of all parameters, the size of the residual triangle is $\leq$ 0.2 arcsec (rms), which is the characteristic length for the error of the relative pointing. The six measured radii are stable and self-consistent with a typical error of the order of 0.5 arcsec with the biggest contribution being a systematic error in the fit of the limb position on the CCD. This error cancels for the reconstruction of the pointing direction. Moreover, it has been shown that the structure of the imager is stable.

2.4.2. Sensitivity
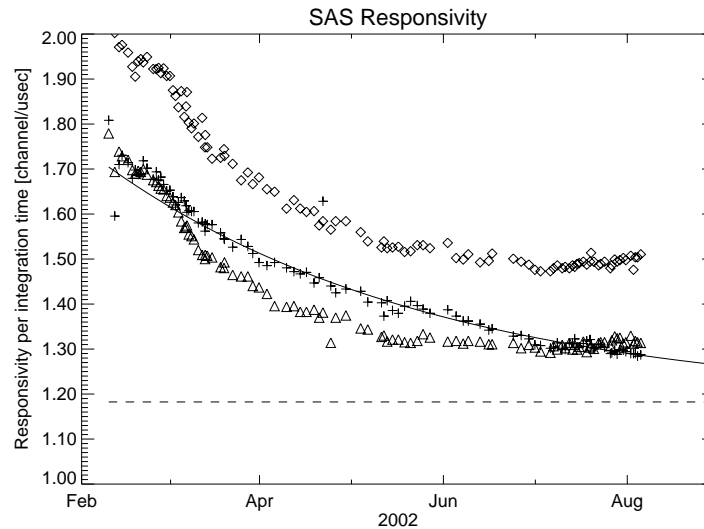
Figure 3. The responsivity for each of the three SAS subsystems is measured in channels per μsec. The crosses indicate the measurements for SAS 1, the triangle for SAS 2 and the diamonds stand for SAS 3. The fitted curve for SAS 1 is an exponential with its asymtotic limit at $\approx$ 1.18 channels/μsec (dashed line).

The SAS lenses and filters[7] has been design to have a transmission of 1.5% of the intensity at 670 nm with a band width of 12 nm FWHM. The transmissivity has been checked during the ground calibration process to have a maximum response at channel $\approx$ 900 on the 10 bit ADC using the nominal integration time of 500 μs. For a given time, the telescope axis can point off the Sun center by as much as 14 arcmin. Therefore, the position of a limb on a particular CCD can be different by several arcsec between two consecutive integration samples using the fixed cadency of the sensors of 128 Hz. The nominal integration time has been chosen to be small enough in order to prevent additional smearing of the limbs during integration.

Fig. 3 shows the measured responsivity for each of the three SAS subsystems in channels per μsec integration time. For instance, with a responsivity of 1.5 channels/μs an integration time of 600 μs is needed in order to get a response of 900 channels. It can be clearly seen that the responsivity for all three SAS's decayed about 25% in the first five month of the mission. It is believed to be due to contamination issues. Furthermore, the outgasing of the whole volume of the imager tube flew through the chemneys in front of the SAS lenses which were completely uncovered since launch.[7]

For SAS 2 and 3, the degrading of the optics has stabilized within the first five month of the mission, whereas the responsitity for SAS 1 is still degrading. In Fig. 3 the data for SAS 1 is shown with an exponential fit excluding the data for the first month. The dashed line shows its asymtotic value as the current best guess

for the lowest level to be reached, which is by far in the acceptable range in order to maintain the accuracy of the system.

3. ROLL ANGLE SYSTEM (RAS)

3.1. RAS principles

The RAS is a star scanner pointing radially outwards with respect to the rotating spacecraft and observes stars within the field of view of 30 degrees in polar angle.[7] Stars within the field of view are focused by a lens system. While the spacecraft is rotating, the images of the stars are traveling over a linear CCD array and are triggering one or several pixels. The plots in Fig. 4 illustrate the geometry in RHESSI-centric coordinate systems. Almost 2π of the sphere are covered by the Earth. At the moment the Earth is within the field of view of the RAS, the sensor can be as much as 1000 times saturated because of the Earth albedo. Since the selected CCD has no anti-blooming capability, a special Earth albedo trigger mechanism had to be implemented in order to remove the accumulated charge on the CCD. This mechanism introduces an additional sensor dead time after rotating out of the Earth albedo of up to 0.8 sec.
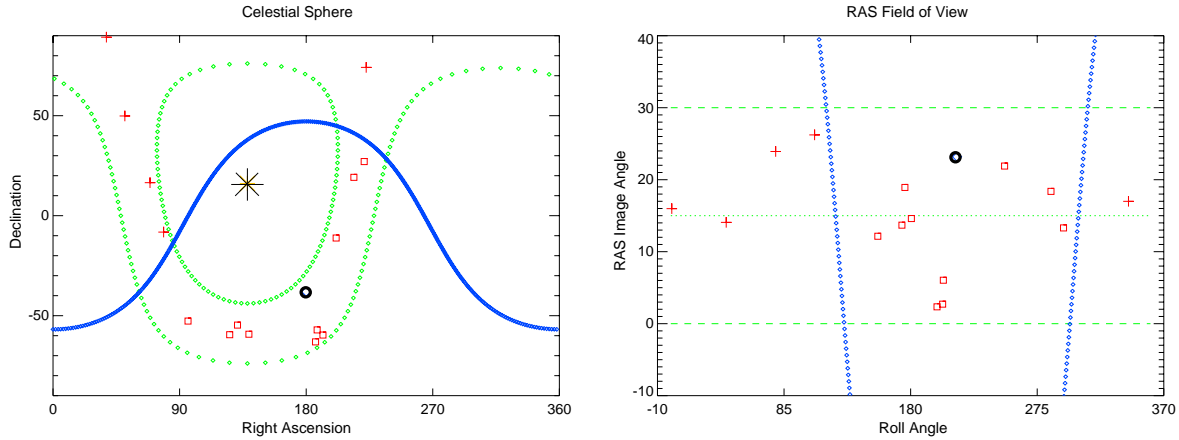

Figure 4. In the left plot, the celestial sphere seen from the spacecraft is shown at a particular time. The star indicates the position of the Sun and the circle indicates the position of the Earth. The concentric dotted lines 'around' the Sun position mark the border of the FOV and the concentric line 'around' the Earth position marks the horizon. In the right plot, the same geometry is shown as seen by the RAS. Note that the Earth horizon corresponds to the almost vertically dotted lines. In both plots, the stars which are seen within a revolution are indicated by crosses and the stars which are in the FOV but hidden by the Earth are indicated by squares.

3.2. Star observation statistics

The required accuracy for the roll angle determination can only be achieved if a sufficient number of stars per revolution are observed. Therefore, extensive modeling of the star observation capability was done based on the Hipparcos input star catalogue. The model contains all necessary elements for the orbit (to be conservative: 38 inclination, 500 km altitude and a 50 km high opaque 'atmosphere', variable right ascension of the ascending node) and for all relevant celestial objects over the year 2001. The Earth occultation is calculated based on the detailed baffle geometry and a conservative afterglow dead time of 0.8 s has been assumed. The point spread function of a star image has been taken from our calibration measurements as ≈ 1 pixel (rms), independent of angle, while for lens vignetting the Leica prediction has been used. The result of the calculation is expressed as fractional blind time, i.e. the number of RHESSI revolutions with no star detected divided by the total number of revolutions, as a function of the threshold. Only those parts of the full orbit were considered when RHESSI is in direct Sun light. The curves shown in Fig. 5 represent an upper limit, since the envelop for all curves has been taken by varying the right ascension of the ascending node over 360 degrees. Although, the dependency of

the fractional blind time from the momentary right ascension of the ascending node is fairly small, the effective value depends on launch time and the precession of the orbit. The calculations were done for the case with no spatial summation (dashed curve) and with spatial summation over 2 adjacent pixels (solid line), demonstrating the considerable improvement, which can be gained by spatial summation. Given the measured noise $\sigma_{rms} <$ 0.7 ch and the requirement that the threshold be at least $5 \cdot \sigma_{noise}$ above dark signal in order to limit the number of random noise events, a reasonable choice for the threshold is about 4 ch. This results in a fractional blind time of about 0.1% (solid line) or 0.7% (dashed curve). Summation over three adjacent pixels yielded a marginal improvement.
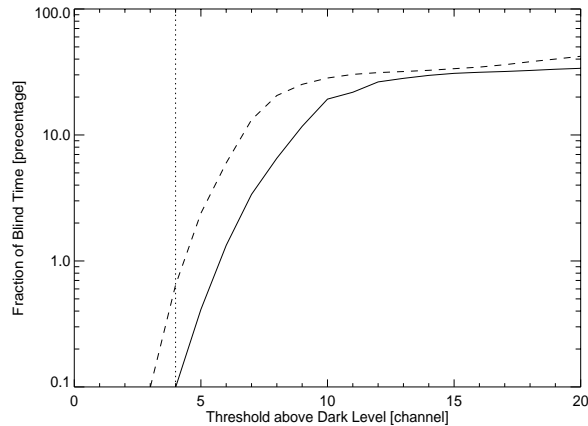
Figure 5. Fractional blind time versus threshold level for the year 2001. The dashed curve was obtained without spatial summation, the solid curve for spatial summation over 2 pixels. The vertical dotted line represents a reasonable threshold setting to be expected.

3.3. Ground calibration

For on-ground calibration, the fully assembled flight model of the RAS has been taken to Jungfraujoch, Switzerland, at an altitude of 3500 m above sea level. This location has the potential of better atmospheric 'seeing' combined with the beneficial side effect of convenient cooling of the CCD. The RAS was mounted on a horizontally rotating support and could be set to scan the sky continuously over about 50 degrees between two end switches. The scanning speed was 30 to 90% of the nominal rotational speed, resulting in a star passage at 35 degrees elevation between 21 ms and 65 ms. This corresponds to 4 to 9 time frames for an integration time of 8.8 ms. The elevation was adjusted manually and kept constant during a measurement. In order to get enough information for fitting of the point spread function, the number of pixels to the left and right of a triggered pixel was set to 10. To check on the stability of the dark signal, mixed event/image mode was implemented and the CCD temperature was constantly monitored and found to be stable between 0 and 5 degreeC.

It has been shown, that the focal length can be optimized for events along the optical axis to yield a point spread of < 1.2 arcmin (FWHM) but increasing to several arcmin for events at up to 15 degrees off-axis.[13] Nevertheless, the fully integrated flight model, which has a fixed focal length, showed a slightly different point spread function which has been found to be constant over the full field of view with a FWHM of 2.1 arcmin.

Star observation on ground is hampered by atmospheric attenuation - loosely speaking clouds and haze - and by effects usually found in the literature under 'seeing', 'stellar scintillation' or 'twinkling'. The first effect produces a net reduction of the light intensity reaching the instrument while the latter may introduce an intensity spread as well as a wavelength re-distribution if one performs a series of independent measurements with short integration time (e.g. see Ref.14). Knowing the characteristics of all the elements of the RAS optics[15] and taking into account the spectral type of the different stars as well as the spectral responsivity of the CCD, the expected response for each star has been calculated. The measured response for many different objects with

visual magnitudes between $m_V=0$ and $m_V=3$ agreed with the expectation and showed usually a signal of 75% to 100% of the expected value. An example of an especially low response of 60% is believed to be explained by clouds and haze and an exception of a high response of 156% is believed to be explained by a exceptionally big uncertainty in the fit of the response because of the very weak signal of the particular faint star with magnitude $m_V=3.65$.

3.4. Preliminary results for flight calibration
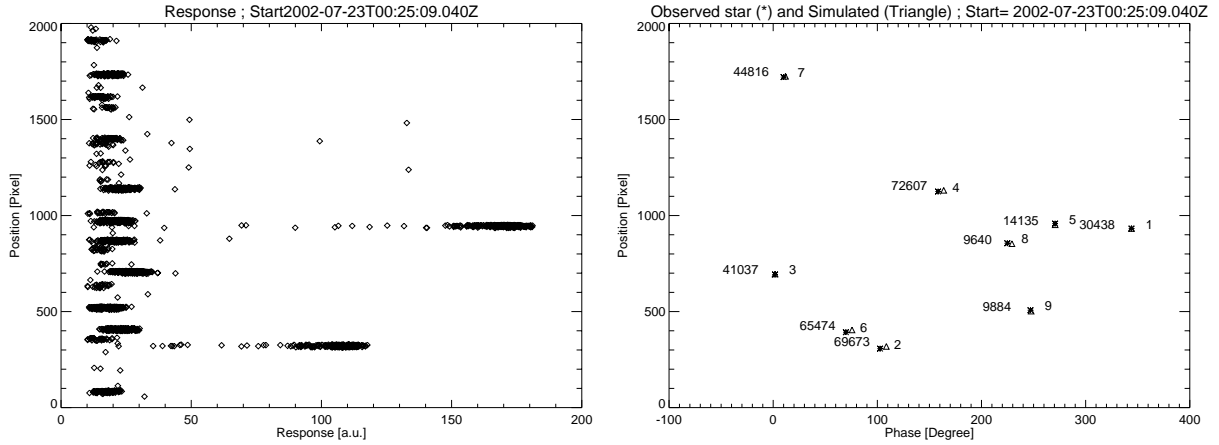
Figure 6. The left plot shows the response (x-axis) for every observed star event vs. the pixel position on the CCD. The right plot shows a map of observed events (asterisks) and predicted stars (triangles) in coordinates of pixel position and roll phase. To the left side on each mark the hipparcos run number is printed.

As has been pointed out in section 3.2, the triggering threshold for RAS events has be at $\approx 5 \cdot \sigma_{noise}$ in order to be sensitive enough and at the same time having the false event rate triggered by noise to be low enough. There are two more effects making the setup of the RAS instrument and the data analysis more difficult. The threshold level to trigger the earth albedo has to be set close to the dark signal in order to trigger all the various levels of earth albedo. On the other hand, the overall level of the dark signal seems to be raised by several channels for a considerably long time after the sensor recovers from the earth albedo and also before rotating into the earth albedo. Those effects together cause a much higher false trigger rate in the flight data than has been expected and therefore a sophisticated cleaning algorithm is required. The cleaned events must yield the following criteria:

1. The passage time of a star image over the CCD is between 15.3 and 17.6 ms (at 15 RPM) whereas the sampling time is ≈ 8.8 ms. Therefore, a star event should trigger pixels at 2 or 3 time frames consecutive in time, but never at more than 3.

2. The time frame with the largest amplitude defines the response of the star. The star light for the full 8.8 ms integration time must illuminate the CCD, since the integration time is less than 1/2 of the passage time.

3. The point spread function if the RAS is about 2 pixels (FWHM), therefore star events should have more than one pixel above threshold.

4. The amplitude of a star should match the calculated amplitude up to a constant factor.

5. The star signal should be repetitive with the spin period of the spacecraft.

6. The phase and pixel position should correspond to a real star.

Currently, the following steps are implemented in order to separate the real star events from the background:

1. Grouping the events according to the number of consecutive time frames, i.e. all events not preceded or followed by another time frame, all events with 2 consecutive time frames, and so on. Ideally the real star events have 2 and 3 time consecutive frames. However, faint stars producing weaker signals may trigger only on time frame.

2. Least square fit of the pixel position of the triggered pixel of each time frame with a Gaussian like function plus a constant background. The background is mostly defined by the adjacent pixels below threshold which are also included in the data stream (currently 3 pixels on either side).

3. Determination of the amplitude of a grouped star events by choosing the maximum amplitude.

4. The fraction of the RAS time of the events modulo the spin period of the spacecraft must be constant for a constant, unknown spin period. This fraction corresponds to the roll angle. The period is varied until the fraction is constant in a predefined time (order of minutes).

To illustrate a preliminary reconstruction of the roll angle, 2000 seconds of data taken during the X-class flare on July 23 at 00:25:09UT has been analyzed. In a first step, the data has been reduced as explained above and 11 stars have been filtered out from the triggered events. These stars have to match stars in the field of view of the RAS with a given response. Assuming that the imaging axis of the telescope is pointing at the Sun, without earth occultation and the minimum response of the stars equals to 80% of the smallest star observed we found 57 candidates of stars to match the 11 observed events. Since the roll angle is completely unknown and the polar angle is only approximately known, the roll angle and the polar angle of the brightest observed star has been fixed to the brightest predicted star. The chi-square using the polar and roll angle and the responses of the remaining combination of the 10 observed events to the 56 predicted stars were evaluated. The star combinations with acceptable chi-square are shown in Fig. 6. The agreement between the observation and the prediction is not perfect since the off-pointing from the Sun center and some offsets in the alignment of the sensor is not anticipated at this point. Using estimations for the spin period for intervals of 100 sec duration, the spin period and the phase is calculated for each star. Fig. 7 shows the residuals to a linear fit to the final calculation of the roll angle illustrating the self-consistency of the data.
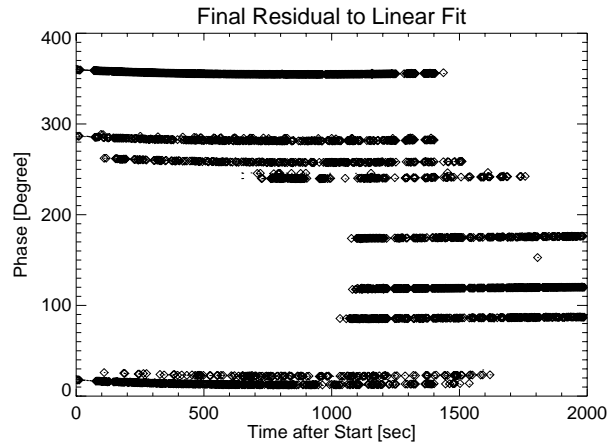
Figure 7. Using an estimation of the spin period for time intervals of 100 sec, the spin period and the phase of each observed star is calculated. The plot shows the residuals to a linear fit to the calculated roll angle for each star event as a function of time.

REFERENCES

1. R.P. Lin et al, "The High Energy Solar Spectroscopic Imgager (HESSI) Small Explorer mission for the next (2000) solar maximum", SPIE Proc. 3442, 2-12, 1998.

2. T.A. Prince, G.J. Hurford, H.S. Hudson and C.J. Crannell, "Gamma-ray and hard X-ray imaging of solar flares", Solar Physics 118, 269-290, 1988.

3. L. N. Mertz, G. H. Nakano and J. R. Kilner, "Rotational aperture synthesis for X-rays", A: Optics and Image Science, 3, 2167-2170, 1986.

4. D. M. Smith and the HESSI Team, "The HESSI Spectrometer, ASP Conference Series", R. Ramaty and N. Mandzhavidze, 206, 2000.

5. D. M. Smith et al, "The RHESSI Spectrometer, to be published in Solar Physics", 2002.

6. K. Thomsen, J. Bialkowski, F. Burri, M. Fivian, W. Hajdas, A. Mchedlishvili, P. Ming, A. Zehnder, "Calibrating the imaging system of the high-energy solar spectroscopic imager (HESSI)", SPIE Proc. 4012, 524-529, 2000.

7. A. Zehnder et al, "RHESSI Imager and Aspect Systems", SPIE Proc. 4853, Waikoloa, Hawaii, 2002.

8. M. Fivian, A. Zehnder, "The RHESSI Imager and Aspect Reconstruction", to be published in Solar Physics, 2002.

9. G. Hurford, E. Schmahl et al, "Imaging Concept", to be published in Solar Physics, 2002.

10. R. Henneck, J. Bialkowski, F. Burri, M. Fivian, W. Hajdas, A. Mchedlishvili, P. Ming, K. Thomsen, J. Welte, A. Zehnder, B.R. Dennis, G. Hurford, D. Curtis, D. Pankow, "The Solar ASpect System (SAS) for the High Energy Solar Spectroscopic Imager HESSI", SPIE Proc. 3765, 771-776, 1999.

11. P. Seige and G. Ress, "Application of Texas Instruments TC-104 linear CCD arrays in spaceborne camera systems", Optical Enginerring, 26(10), 1029 - 1034, 1987.

12. G. J. Yates et al, "Characterization of electro-optic anomalies associated with transient responses of fast readout charge-coupled devices", Optical Engineering, 26(8), 747 - 756, 1987.

13. M. Fivian et al, "Calibrating the aspect systems of the high energy solar spectroscopics imager (HESSI)", SPIE Proc. 4012, 518-523, 2000.

14. E. Jakeman et al, "The Twinkling of Stars", Contemp. Phys., 19(2), 127-145, 1978.

15. R. Henneck, J. Bialkowski, F. Burri, M. Fivian, W. Hajdas, A. Mchedlishvili, P. Ming, K. Thomsen, J. Welte, A. Zehnder, M. Dettwyler, F. Bürki, G. Hurford, D. Curtis, D. Pankow, "The Roll Angle System (RAS) for the High Energy Solar Spectroscopic Imager HESSI", SPIE Proc. 3765, 518-523, 1999.